PAPER

SFX as a low-cost 'Spiro' hole-transport material for efficient perovskite solar cells†

Michal Maciejczyk, Aruna Ivaturi and Neil Robertson*

Four spiro[fluorene-9,9′-xanthene] (**SFX**) derivatives, **SFX-TAD**, **SFX-TCz**, **SFX-TPTZ** and **SFX-MeOTAD** have been synthesized for use as hole-transport materials and fully characterized by $^1H/^{13}C$ NMR spectroscopy, mass spectrometry, XRD and DSC. Their thermal, optical and electrochemical properties were investigated. The use of different substituents affects the highest occupied molecular orbital (HOMO) energy level proving the versatility of the central core towards the facile and low-cost preparation of spiro-hole-transport materials. Among the synthesized **SFX** derivatives, **SFX-MeOTAD** was employed as hole-transporting material (HTM) and the performance tested in perovskite solar cells with device architecture glass/FTO/compact TiO_2/mesoporous Al_2O_3/$CH_3NH_3PbI_{3-x}Cl_x$/HTM/Au. **SFX-MeOTAD** gave a comparable efficiency to **spiro-MeOTAD**, demonstrating great potential for use of the **SFX** family as cost effective and versatile hole conductors facilitating commercialization of perovskite solar cells (PSCs).

1 Introduction

Lead halide perovskite was first introduced to photovoltaics as a sensitizer in dye-sensitized solar cells by Miyasaka.[1] This material type has since attracted huge attention due to outstanding properties including high extinction coefficient, small exciton binding energy, long charge carrier diffusion length and lifetime. In consequence, 21% certified efficiency by EPFL has been recently achieved.[2] The most common structure of perovskite solar cells (PSCs) includes **spiro-MeOTAD** as a hole conductor but its high price and tedious multistep synthesis hinders progress of this technology towards commercialization. There is therefore a requirement for alternative hole transporting materials (HTMs), which should fulfil the following demands: matching the energy levels of the active layer, forming smooth and stable films, good solubility for solution-processed devices, low-cost production and high hole conductivity.

Many small molecules, polymers and inorganic salts have been explored as HTMs but small molecules tend to be more attractive due to ease of purification, high purity and smaller batch-to-batch variation. The most recent reports on high efficiencies of PSCs with small organic molecules as hole-transporting materials include structures like: methoxydiphenylamine-substituted carbazole (V886),[3] triazatruxene (TPDI),[4] (KR131),[5] [2,2]para-cyclophane triarylamine (PCP-TPA),[6] azomethine[7] and diacetylide-triphenylamines (DATPA).[8] Efficiencies comparable with **spiro-MeOTAD** have been shown and also improvement of thermal stability, simpler preparation methods and total cost of synthesis. In nearly all these cases however, there has been no development of a wider family of materials with differing redox potential, solubility or thermal properties, although this is likely to prove important to enable better-matched combination with differing perovskite materials.

Most of the reported small molecule based HTM materials have a nonplanar 3D architecture, which can reduce electronic coupling and charge recombination,[9] provide high thermal stability, high glass transition temperature and favourable solubility. One of the key methods to achieve such properties is the utilization of a central spiro carbon, as demonstrated by the ubiquitous **spiro-MeOTAD** where two fluorenes are orthogonally interconnected. To overcome the high cost and complexity of spiro-bifluorene synthesis however, in the present study we have focussed our interest on spiro[fluorene-9,9′-xanthene] **SFX** due to its easy synthesis which was reported as an "Unexpected One-Pot Method…".[10] This core has attracted a lot of attention recently as a starting material for "eco-friendly green organic semiconductors"[11] but work has so far been limited mainly to light emitting diodes (OLEDs).[12–16] Surprisingly, among the reported structures and their high complexity, no tetraamino substituted derivatives have been described. An additional motivation for our interest in the target molecule was a study by Koene *et al.*[17] showing thermal stability enhancement of asymmetric triaryldiamines for hole transporting layer in OLEDs over the symmetric ones with maintenance, or improvement, of other desired properties.

School of Chemistry and EaStCHEM, University of Edinburgh, King's Buildings, West Mains Road, Edinburgh, Scotland EH93JJ, UK. E-mail: Neil.Robertson@ed.ac.uk

† Electronic supplementary information (ESI) available: Additional electrochemical measurements of **SFX** derivatives, DSC curves, cost estimation, extended crystallographic table and X-ray structures, ^1H and ^{13}C NMR, COSY, NOESY and HSQC spectra for all synthesized compounds. CCDC 1443037, 1443041 and 1443040. For ESI and crystallographic data in CIF or other electronic format see DOI: 10.1039/c6ta00110f

This journal is © The Royal Society of Chemistry 2016

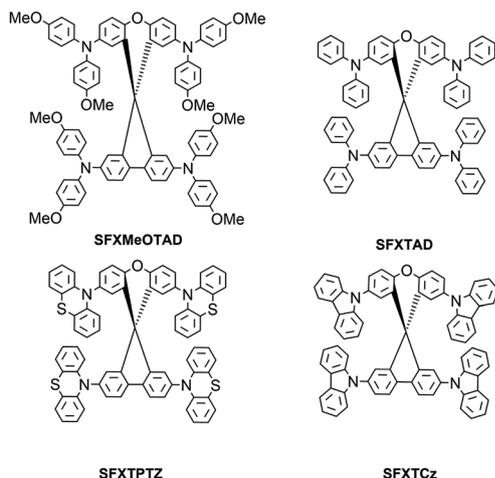*J. Mater. Chem. A*, 2016, **4**, 4855–4863 | 4855

Fig. 1 Chemical structures of SFX based hole conductors.

Herein, we report the facile synthesis of four new SFX-based hole conductors, as shown in Fig. 1, with a variety of HOMO energy levels to achieve redox tuning. Among them, we have so far studied SFX-MeOTAD in detail for application in perovskite solar cells. This material shows high glass transition temperature, high solubility, purely amorphous state and HOMO level alignment almost identical to spiro-MeOTAD. We show that devices employing SFX-MeOTAD show high power conversion efficiency up to 12.4%, compared with 13.0% for spiro-MeO-TAD, but with the significant advantage of more than 5 times lower cost of synthesis. Furthermore, the easy synthesis of this series has enabled us to prepare examples of varying redox potential, offering a choice of HTM tailored to other emerging perovskite solar cell materials.

2 Results and discussion

2.1 Synthetic procedures

The synthetic procedure for the preparation of SFX derivatives is shown in Fig. 2. The key step is the synthesis of the central core spiro[fluorene-9,9′-xanthene] (SFX). In contrast to 9,9′-spirobifluorene (SBF), where only multistep protocols were reported[18–21] involving Grignard reaction demanding dry solvents, the procedure for SFX is a one-pot, non-solvent synthesis which was reported previously.[10] Moreover, reagents (phenol and methanesulfonic acid) are more than 30 times cheaper than 2-bromobiphenyl or 2-iodobiphenyl used in SBF synthesis. Scaling up the reaction to produce about 50 g of SFX only

slightly decreased reaction yield from 80% to 77% even though the column purification was replaced by a silica plug followed by recrystallization from ethanol/methanol. Tetrabromination was conducted in excess bromine with high yield of 75% at the scale of 40 g of starting material. The only purification used was a silica plug followed by recrystallization from chloroform/ethanol mixture. Various molecular designs of the new hole conductors based on carbazole, diphenylamine, 4,4′-dimethoxydiphenylamine and phenothiazine motifs were synthesized by the Buchwald–Hartwig amination reaction between 2,2′,7,7′-tetrabromo-spiro(fluorene-9,9′-xanthene) and the respective amine. Final products were isolated with 71%, 56%, 35%, 83% yield for SFX-MeOTAD, SFX-TAD, SFX-TPTZ and SFX-TCz, respectively. Column chromatography was used for all final product purifications except SFX-TPTZ where crystallization from toluene/chlorobenzene was applied. Additionally, two amination conditions were tested for SFX-MeOTAD and the more economic tri(o-tolyl)phosphine and $Pd_2(dba)_3$ instead of tri-tert-butylphosphonium tetrafluoroborate and $Pd(OAc)_2$ gave similar reaction yield of about 60% at small scale. Scaling up this reaction with the use of palladium(II) acetate as a catalyst to 7 g of starting SFXTBr increased the reaction yield to 71% and 2.568 g of 4,4′-dimethoxydiphenylamine were recovered. All of the analytical data ($^1H/^{13}C$ NMR spectroscopy and mass spectrometry, see ESI†) support the proposed structures. Additionally, solubility of SFX-MeOTAD was found to be more than 300 mg mL^{-1}, similar to spiro-MeOTAD[22] but with much faster dissolution than spiro-MeOTAD. Full experimental details and characterization can be found in the experimental section.

2.2 Cost analysis

As previously mentioned by Murray et al.,[23] large-scale production of solar cells is hindered by the cost of spiro-MeOTAD. In particular, the SBF core and the Pd-catalysed coupling are the main influence on the final price of the material. In Table S1† it can be seen that the cost of materials for the synthesis of SBF, ranging from $35 to $44 per gram, is responsible for about half of the final cost of spiro-MeOTAD. Therefore, the introduction of SFX core as an inexpensive alternative (costing about $1 per gram) cuts the cost of the final material to half and decreases the number of steps from 6 for spiro-MeOTAD to 3 for SFX-MeOTAD (see Fig. S6†). Further optimization and scaling up the synthesis of SFX-MeOTAD gave a final cost of the new hole conductor more than five times lower (17$) [see Tables S2–4†] than the commonly used spiro-MeOTAD (from 92$ to 108$).[7] Additionally, the availability of the new cost-effective core for
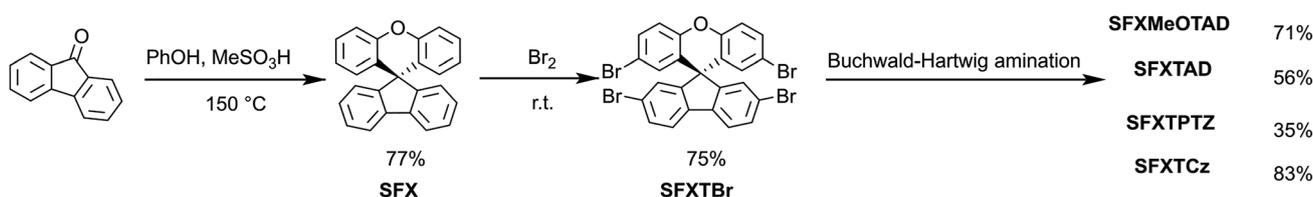

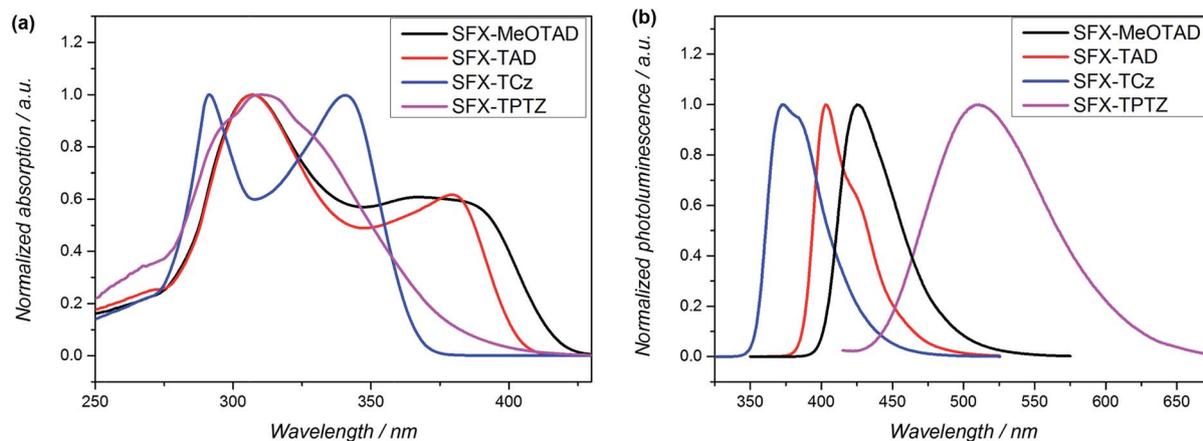Fig. 2 Synthetic route for SFX and its derivatives.

Fig. 3 (a) Normalized UV-visible absorption in DCM at 2×10^{-5} mol mL^{-1}. (b) Photoluminescence in DCM at 5×10^{-6} mol mL^{-1} of **SFX** series.

hole transport materials that has similar electronic properties to SBF, can open up more diverse modification with other diphenylamine derivatives beyond 4,4′-dimethoxydiphenyl-amine[23,24] that can benefit device stability or efficiency through tailoring hole-transport materials according to the energy levels of the chosen perovskite.

2.3 Optical and electrochemical properties

The UV-vis absorption spectra of the **SFX** series in dichloromethane (DCM) are presented in Fig. 3a. All derivatives show an absorption in the UV region. **SFX-MeOTAD**, **SFX-TAD** and **SFX-TCz** exhibit two absorption bands at 307, 367; 307, 379 and 291, 340 nm, respectively whereas **SFX-TPTZ** shows one broad absorption band with maximum at 310 nm. Photoluminescence spectra are depicted in Fig. 3b.

The maximum of the emission is red-shifted in the following order: **SFX-TCz** (372 nm), **SFX-TAD** (403 nm), **SFX-MeOTAD** (425 nm) and **SFX-TPTZ** (509 nm). Optical band gaps shown in Table 1 were estimated from the absorption onset. The maxima of absorption and emission of **SFX-MeOTAD** are similar to **spiro-MeOTAD** resulting in the same value of optical band gap for both materials. Stokes shifts were calculated from the difference between the maximum of absorption and emission

spectra. The largest Stokes shift was observed for **SFX-TPTZ** (12 600 cm^{-1}), indicating a greater geometric difference upon relaxation of the excited state compared with the ground state. Additionally, broad absorption and emission bands with planar type structure of the phenothiazine suggest formation of twisted intramolecular charge transfer (TICT) state as is observed for example for 9,9′-binathryl.[25] On the other hand, small Stokes shift and narrow bands for **SFX-TCz** imply that this nonradiative channel is not accessible regardless of the planarity of carbazole and previously-reported[26] TICT behaviour for this kind of structure.

The highest occupied molecular orbital (HOMO) energy levels of the compounds were estimated from the half-wave potential using ferrocene/ferrocenium as an internal standard in cyclic voltammetry (Fig. 4a) and square-wave voltammetry (Fig. 4b) experiments. The first oxidation potential of **SFX-MeOTAD** was found to be almost the same as **spiro-MeOTAD**; therefore the energy of the HOMO levels of both materials are about −5.1 eV. Whereas, **SFX-TAD**, **SFX-TCz** and **SFX-TPTZ** have higher oxidation potentials thus lowering their HOMO levels to −5.34, −5.70 and −5.39 eV respectively.

From the CV measurements, it can be noted that **SFX-MeOTAD** exhibits three reversible oxidation peaks and on the SWV graph the comparison to the 'Spiro' shows that first and third

Table 1 Electrochemical, photophysical and thermal properties

HTM	λ_{max} (nm)	λ_{em}[a] (nm)	Stokes shift[b] (cm^{-1})	E_{gap}[c] (eV)	E_{ox}[d] (V)	E_{HOMO}[e] (eV)	E_{LUMO}[f] (eV)	T_g[g] (°C)	T_m[g] (°C)
Spiro-MeOTAD	301, 385	424	9640 (2390)	2.98 (ref. 34)	(+0.04)	−5.14 (−5.15) (ref. 35)	−2.16 (2.11) (ref. 35)	122 (125) (ref. 36)	248 (248) (ref. 36)
SFX-MeOTAD	307, 367	425	9040 (3720)	2.96	+0.07 (+0.05)	−5.16	−2.20	108	237
SFX-TAD	307, 379	403	7760 (1570)	3.07	+0.23 (+0.26)	−5.34	−2.27	118	245
SFX-TCz	291, 340	372	7480 (2530)	3.39	+0.60	−5.70	−2.31	—	>270
SFX-TPTZ	310	509	12 600	3.25	+0.27 (+0.32)	−5.39	−2.14	—	>270

[a] Excitation at bold λ_{max}. [b] The difference between the maximum of absorption and maximum of emissions spectra; in parenthesis is the difference between lower energy absorption bands and maximum of emission spectra. [c] From the absorption onset. [d] The half-wave potential from the CV and in parentheses the peak potential from the SWV measurements referenced to ferrocene. [e] E_{HOMO} (eV) = −5.1 − (E_{ox}).[37] [f] $E_{LUMO} = E_{HOMO} + E_{gap}$. [g] Determined by differential scanning calorimetry (DSC).

This journal is © The Royal Society of Chemistry 2016

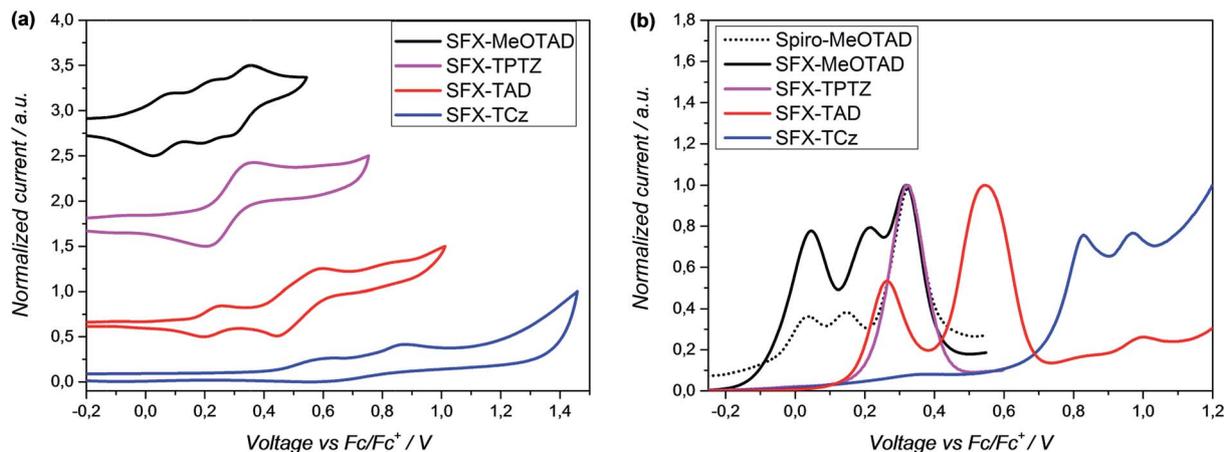J. Mater. Chem. A, 2016, **4**, 4855–4863 | **4857**

Fig. 4 (a) Cyclic voltammograms (CV) and (b) square-wave voltammetry (SWV) traces of the **SFX** series and **spiro-MeOTAD** in DCM solution with supporting electrolyte 0.3 M tetrabutylammonium tetrafluoroborate referenced to ferrocene.

are at the same potential. Oxidation reversibility of all studied hole conductors was confirmed (see ESI, Fig. S1 and S2†). Overall these results indicate that the hole transfer from $MAPbI_{3−x}Cl_x$ to the new HTM materials should be favourable, except for **SFX-TCz**. Moreover, the lower HOMO energy level for **SFX-TAD** and **SFX-TPTZ** could potentially lead to higher open circuit voltages of the operating devices. At present, poor solubility of these latter materials hinder their application in solar cells, and synthesis of more-soluble analogues is required to test this hypothesis. Table 1 summarizes the optical and electrochemical properties of the materials in comparison to the **spiro-MeOTAD**.

2.4 XRD analysis

The structures of the new materials have been confirmed conclusively by X-ray diffraction analysis of three of them as shown in Fig. S4.† The compounds were found to crystallize in triclinic space group $P\bar{1}$ (**SFX-MeOTAD**), monoclinic $C2/c$ (**SFX-TPTZ**) and orthorhombic $Pbca$ (**SFX-TCz**). In Fig. 5, we can see that **SFX-MeOTAD** forms three types of hydrogen bonds with lengths of 2.522 Å for CHO (xanthene), 2.549 Å and 2.572 Å for OMe–OMe. The dihedral angle between fluorene and xanthene units was measured to be 87.54°, 88.89° and 87.57° respectively for **SFX-MeOTAD**, **SFX-TPTZ** and **SFX-TCz** (see ESI, Fig. S7 and S8†). This is similar to the value found for **spiro-MeOTAD** (89.94°)[27] which is the origin of low intermolecular interactions and therefore the formation of stable amorphous solids. Taking into account that **SFX-MeOTAD** has the same peripheral groups (*i.e.* 4,4′-dimethoxydiphenylamine) and crystallizes in P$\bar{1}$ space group as does **spiro-MeOTAD**, a similar amorphous state would be expected. On the other hand, for **SFX-TPTZ** π–π interactions with length of 3.756 Å and for **SFX-TCz** 3.868 Å and 3.752 Å were observed (Fig. S5†). Which is in agreement with higher melting points and lower solubility for both of materials indicating strong intermolecular interaction.

The X-ray powder diffraction patterns on the bulk samples (as synthesized) were experimentally obtained and compared with the simulated ones from their single-crystal data (Fig. S9†).

Importantly, the powder pattern for **SFX-MeOTAD** showed the presence of only the amorphous state whereas the **spiro-MeO-TAD** pattern indicated some crystallinity in agreement with the simulated pattern. Greater crystallinity in the powder samples was observed for **SFX-TPTZ** and almost pure crystal form for **SFX-TCz**. Interestingly, the experimental data for **SFX-TAD** showed that the introduction of methoxy groups has an influence, as expected, on readily obtaining an amorphous state since some peaks were observed for the unsubstituted derivative. The summary of X-ray crystallographic data for **SFX-MeOTAD**, **SFX-TPTZ** and **SFX-TCz** is given in ESI Table S5.†
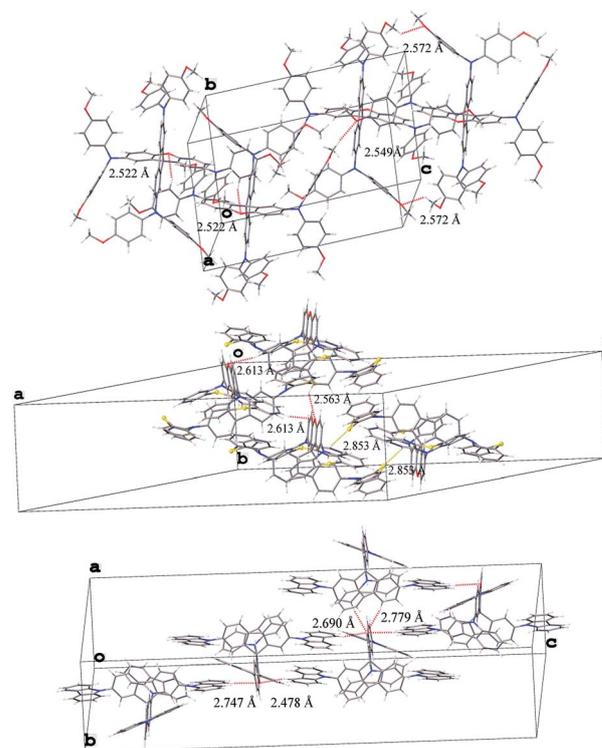

Fig. 5 Crystal packing of **SFX-MeOTAD**, **SFX-TPTZ** and **SFX-TCz**.

4858 | *J. Mater. Chem. A*, 2016, **4**, 4855–4863

This journal is © The Royal Society of Chemistry 2016

2.5 Thermal properties

The results from Differential Scanning Calorimetry (DSC) are shown in ESI (Fig. S3–5†). DSC data show glass transition temperature (T_g) of 108 °C, 122 °C and 118 °C for **SFX-MeOTAD**, **spiro-MeOTAD** and **SFX-TAD**, respectively. The three materials show cold crystallization: **SFX-MeOTAD** at 197 °C, **spiro-MeO-TAD** at 176 °C and **SFX-TAD** at 178 °C. For **SFX-TPTZ** and **SFX-TCz** neither T_g nor melting point (T_m) up to 270 °C were observed. This may be associated with the strong intermolecular interactions observed by single-crystal X-ray diffraction and the high crystallinity seen in powder diffraction experiments.

Similarly to the powder diffraction results, better packing of **SFX-TAD** manifests in not only higher T_g but melting point as well, raising it from 237 °C for **SFX-MeOTAD** to 245 °C for **SFX-TAD** (although an additional smaller endothermic peak is observed at 221 °C). The experiment conducted on **spiro-MeO-TAD** shows higher melting point of 248 °C. These results confirm the conclusion that **SFX-MeOTAD** forms stable amorphous glasses and has high thermal stability.

2.6 Solar cell studies

In order to investigate the performance of **SFX-MeOTAD** as hole transport material in perovskite solar cells, the following device
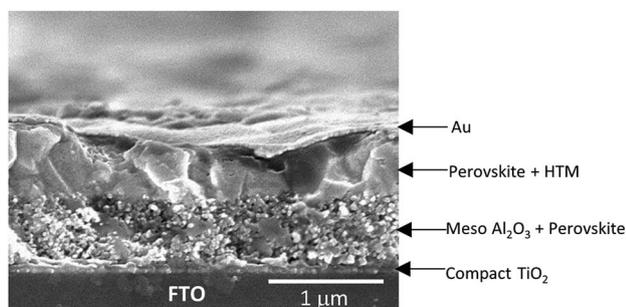

Fig. 6 Cross-sectional SEM image of a typical $CH_3NH_3PbI_{3-x}Cl_x$ based PSC.

architecture was adopted in the present study – glass/FTO/compact TiO_2/meso Al_2O_3/$CH_3NH_3Pb_{3-x}Cl_x$/HTM (**spiro-MeO-TAD** or **SFX-MeOTAD**)/Au. Fig. 6 shows the cross-sectional scanning electron micrograph of a typical device clearly showing the different layers present. To enable reliable comparison between **SFX-MeOTAD** and **spiro-MeOTAD**, all PSCs were fabricated in a single continuous study over 12 repeats for each HTM using identical steps and similar concentration of additives [LiTFSI [lithium bis(trifluoromethanesulfonyl)imide] and tBP (*tert*-butylpyridine)] optimised for the later. Fig. 7 shows the *J*–*V* characteristics of the champion devices recorded using 0.05 V s^{-1} from forward bias to short circuit condition. The table in the inset gives the corresponding photovoltaic parameters of the champion devices. The best cell efficiency of 12.4% was obtained using **SFX-MeOTAD** whereas 13.0% was observed for PSC using **spiro-MeOTAD**. The slightly different HOMO and the oxidation potential of **SFX-MeOTAD** as compared to **spiro-OMeTAD** results in slightly higher V_{oc} and lower J_{sc} of the former as compared to the latter. The slightly lower FF on the other hand is related to the high series resistance which in this case would be due to the resistance to transport in the HTM due to slightly different hole conductivity (1.6×10^{-5} S cm^{-1} and 1.4×10^{-5} S cm^{-1} for **spiro-MeOTAD** and **SFX-MeOTAD**, respectively). The values agree well with the values reported for **spiro-MeOTAD** in the literature.[28] The higher FF for **spiro-MeOTAD** may also arise from the use of a dopant regime optimised for that material.[29] Fig. 8 shows the box plots with the mean and standard deviation of the photovoltaic parameters of the devices measured under simulated AM1.5G sunlight at 100 mW cm^{-2} with *J*–*V* curves recorded using 0.05 V s^{-1} from forward bias to short circuit condition. It is interesting to note the high J_{sc} values observed for both **SFX** and spiro based HTMs. The high J_{sc} values could be possibly due to the reduced number of grain boundaries and low dimensional defects due to larger grains (clearly seen in the SEM micrograph in Fig. 6) and increased crystallinity of the perovskite layer due to the solvent annealing step.[30] It is worth noting that the theoretical maximum achievable value for J_{sc} is 26 mA cm^{-2} assuming 100% internal quantum efficiency and 5% optical losses in the FTO.[31]
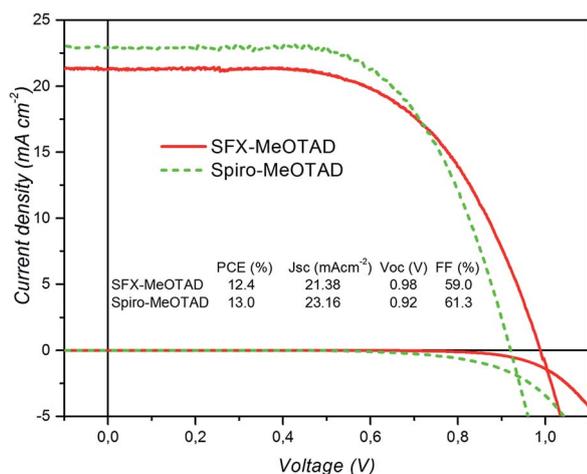

Fig. 7 *J*–*V* curves (light and dark) of the champion PSCs with **SFX-MeOTAD**, and **spiro-MeOTAD** HTMS recorded using 0.05 V s^{-1} from forward bias to short circuit.
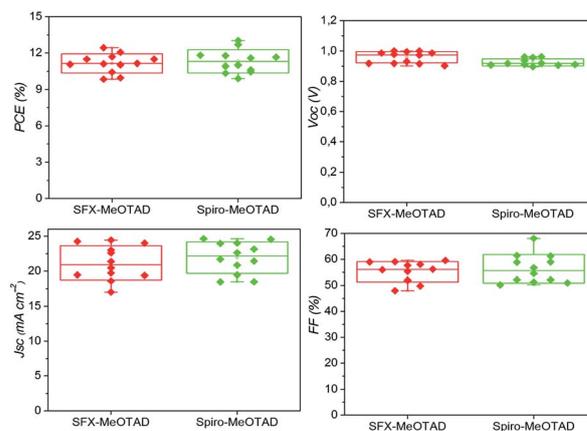

Fig. 8 Box plot of photovoltaic parameters of PSCs with **SFX-MeO-TAD** (left), and **spiro-MeOTAD** (right) HTMS recorded using 0.05 V s^{-1} from forward bias to short circuit.

As expected, PSCs using **SFX-MeOTAD** showed comparable photovoltaics parameters with the mean and standard deviation PCE = $11.1 \pm 0.8\%$, $J_{sc} = 21.2 \pm 2.4$ mA cm^{-2}, $V_{oc} = 0.96 \pm 0.04$ V, FF = $55.2 \pm 3.9\%$ as compared to those using **spiro-MeOTAD** with PCE = $11.3 \pm 0.9\%$, $J_{sc} = 21.9 \pm 2.4$ mA cm^{-2}, $V_{oc} = 0.92 \pm 0.02$ V, FF = $56.4 \pm 5.5\%$. It is important to note that these values correspond to the J–V curves recorded using 0.05 V s^{-1} from forward bias to short circuit condition. The devices exhibit hysteresis, very common in perovskite solar cells and the box plots with the mean and standard deviation of the average PCE (for the forward and reverse direction) of the devices measured under simulated AM1.5G sunlight at 100 mW cm^{-2} with J–V curves recorded using 0.05 V s^{-1} scan speed are shown in the Fig. S11.† PSCs using **SFX-MeOTAD** showed comparable average PCE with the mean and standard deviation PCE = $9.2 \pm 0.9\%$, as compared to those using **spiro-MeOTAD** with average PCE = $9.5 \pm 0.6\%$. The corresponding photovoltaics parameters for the scan direction from short circuit to forward bias condition are given in the ESI (Fig. S10†). The lower PCE values observed for the scan direction when measured from short circuit to forward bias condition are mainly due to the loss in the FF.

3 Conclusions

In conclusion, we have synthesised four novel hole conductors using the **SFX** core for the first time in triarylamine-based materials. This approach significantly reduced the cost of the final material, namely **SFX-MeOTAD**, compared with the commonly-used analogue compound, **spiro-MeOTAD**. The synthesized materials have been characterized using spectroscopic methods, electrochemistry, single crystal and powder diffraction and differential scanning calorimetry. It has been shown that HOMO energy level can be easily modified but at present solubility in the case of **SFX-TCz**, **SFX-TPTZ** and **SFX-TAD** was too low to test these materials in the solar cell devices. Therefore, the material demonstrated for application in perovskite solar cells was **SFX-MeOTAD**, based on its high solubility, highly amorphous state and appropriate HOMO energy level alignment. Comparable tests of the devices' performance confirmed this choice showing a high efficiency of 12.4% for **SFX-MeOTAD** and 13.0% for the reference **spiro-MeOTAD** when measured from the forward bias to short circuit, with average efficiencies for these almost identical. Further investigations on **SFX**-based hole transporting materials are being continued in our laboratory mainly focused on highly processable derivatives with a variety of oxidation potentials. We are confident that this will lead to an improvement in the device efficiency and allow easy tailoring of HTMs to a particular device structure.

4 Experimental

4.1 Materials and synthesis

All reagents were purchased from either Sigma-Aldrich or AlfaAesar and they were used as received without further purification unless otherwise stated. All preparations were carried out using standard Schlenk line and air-sensitive chemistry techniques under nitrogen atmosphere. Toluene was dried using a solvent purification system. Column chromatography was carried out using Silica 60A (particle size 35–70 μm, Fisher, UK) as the stationary phase, and TLC was performed on pre-coated silica gel plates (0.25 mm thick, 60 F254, Merck, Germany) and observed under UV light.

4.2 Chemical characterization

NMR spectra were recorded on Bruker (400, 500 and 600 MHz) spectrometers for solutions in benzene-d$_6$, CDCl$_3$ and methylene chloride-d$_2$. Chemical shifts are reported in parts per million. Chemical shift multiplicities are reported as s: singlet, d: doublet, t: triplet, q: quartet, quint: quintet, and m: multiplet. Mass spectra (EI, ESI) were recorded with Xevo QTOF (Waters) high resolution, accurate mass tandem mass spectrometer equipped with Atmospheric Solids Analysis Probe (ASAP) and Bruker MicroToF 2. Elemental analyses were carried out by Stephen Boyer of the Science Centre, London Metropolitan University using a Carlo Erba CE1108 Elemental Analyser.

4.3 Electrochemical characterization

All cyclic voltammetry measurements were carried out in freshly distilled CH$_2$Cl$_2$ using 0.3 M [TBA][BF$_4$] electrolyte in a three-electrode system, with each solution being purged with N$_2$ prior to measurement. The working electrode was a Pt disk. The reference electrode was Ag/AgCl and the counter electrode was a Pt rod. All measurements were made at room temperature using a mAUTOLAB Type III potentiostat, driven by the electrochemical software GPES. Cyclic voltammetry (CV) measurements used scan rates of 0.1 V s^{-1}; square wave voltammetry (SWV) was carried out at a step potential of 0.004 V, square wave amplitude of 0.025 V, and a square wave frequency of 25 Hz (**SFX-MeOTAD**, **SFX-TAD**), 15 (**SFX-TPTZ**, **spiro-MeOTAD**) and 10 Hz (**SFX-TCz**), giving a scan rate of 0.04 V s^{-1}. Ferrocene was used as the internal standard in each measurement.

4.4 Optical characterization

Solution UV-visible absorption spectra were recorded using a Jasco V-670 UV/vis/NIR spectrophotometer controlled with SpectraManager software. Photoluminescence (PL) spectra were recorded with a Fluoromax-3 fluorimeter controlled by the ISAMain software. All samples were measured in a 1 cm cell at room temperature with dichloromethane as solvent. Concentration of 2×10^{-5} and 5×10^{-6} mol mL^{-1} were used for solution UV/visible and PL, respectively.

4.5 Thermal characterization

Differential scanning calorimetry (DSC) was performed on NETZSCH STA 449F1 at a scan rate of 10 K min^{-1} under nitrogen atmosphere in DSC/TG aluminium pan. The measurement range was 25 °C to 270 °C.

4.6 Crystallographic details

Powder diffraction was performed on a Bruker Discover D8 with CuK$_{\alpha1/2}$ source and a scintillation detector.

4860 | J. Mater. Chem. A, 2016, **4**, 4855–4863

This journal is © The Royal Society of Chemistry 2016

Crystallographic data were collected using Agilent Technologies SuperNova with Cu Kα ($l\frac{1}{4}$1.54178 A) radiation at 120 K. Single colourless block-shaped crystals of **SFX-MeOTAD** were recrystallised from a mixture of DCM, methanol and acetone by solvent layering. Single colourless block-shaped crystals of **SFX-TPTZ** were recrystallised from a mixture of DCM and hexane by solvent layering. Single colourless prism-shaped crystals of **SFX-TCz** were recrystallised from a mixture of hexane and DCM by solvent layering. A suitable crystal of **SFX-MeOTAD** (0.40 × 0.08 × 0.03), **SFX-TPTZ** (0.41 × 0.09 × 0.04) and **SFX-TCz** (0.19 × 0.16 × 0.10) were selected and mounted on a MITIGEN holder in Paratone oil on a Rigaku Oxford Diffraction SuperNova diffractometer. The crystal was kept at $T = 120.0$ K during data collection. Using Olex2 (Dolomanov *et al.*, 2009), the structure was solved with the ShelXS (Sheldrick, 2008) structure solution program, using the direct methods solution method. The model was refined with version of ShelXL (Sheldrick, 2008) using least squares minimisation.

A summary of data collection and structure refinement is reported in Table S5.† The crystal structures were deposited at CCDC with deposition number 1443037, 1443041 and 1443040 for **SFX-MeOTAD**, **SFX-PTZ** and **SFX-TCz** respectively.

4.7 Synthesis and characterization

Spiro[fluorene-9,9′-xanthene] (SFX). A mixture of fluorenone (35.740 g, 198.324 mmol, 1 equiv.), phenol (186.643 g, 19.83 mol, 10 equiv.), and methane sulfonic acid (MeSO$_3$H, $d = 1.48$ g mL^{-1}, 51.48 mL, 79.33 mol, 4 equiv.) was heated at 150 °C under nitrogen for 24 h. The reaction mixture was then slowly added into water (1 L) and extracted with dichloromethane (750 mL). Organic layer was washed with 5% NaOH (300 mL) three times. Then it was filtered through silica plug (120 g) washed with DCM (100 mL). Concentrated on rotary evaporator to give beige solid which was suspended in EtOH (650 mL) and washed with EtOH (3 × 100 mL) and MeOH (100 mL) to afford colorless solid of **SFX** (50.753 g, 77%).

^{1}H NMR (400 MHz, CDCl$_3$, ppm): δ = 7.87 (d, J = 7.6 Hz, 2H), 7.45 (ddd, J = 7.6 Hz, J = 6.4 Hz, J = 2.2 Hz, 2H), 7.32–7.20 (m, 8H), 6.85 (ddd, J = 7.1 Hz, J = 2.3 Hz, 2H), 6.51 (m, 1H), 6.47 (d, J = 1.3 Hz, 1H).

2,2′,7,7′-Tetrabromo-spiro(fluorene-9,9′-xanthene) (SFX-TBr). To a solution of spiro[fluorene-9,9′-xanthene] (40 g, 0.120 mol) in dichloromethane (400 mL) under nitrogen bromine (49.3 mL, 0.963 mol) was added. The resulting mixture was stirred at room temperature for 14 hours. After this time the ^{1}H NMR spectroscopy confirmed forming expected product with no substrate or by-products. The solution was poured on 0.5 L of water, 500 mL of DCM was added and it was washed with saturated sodium thiosulfate (50 g). The organic layer was separated, dried over magnesium sulfate and concentrated on rotary evaporator to about 700 mL. Precipitated in MeOH (500 mL), filtrated and washed MeOH (100 mL) to give white powder of crude product 60.703 g (78%). It was purified by crystallization in 1.6 L of chloroform/ethanol mixture (1 : 1) to give 58.638 g (75%) of white crystalline solid.

Elemental analysis (%). Calculated for C$_{25}$H$_{12}$Br$_4$O: C 46.34, H 1.87. Result: C 46.32, H 1.81.

^{1}H NMR (500 MHz, CDCl$_3$) δ 7.66 (s, 1H), 7.65 (s, 1H), 7.55 (dd, J = 8.2, 1.7 Hz, 2H), 7.34 (dd, J = 8.8, 2.4 Hz, 2H), 7.22 (d, J = 1.7 Hz, 2H), 7.13 (s, 1H), 7.11 (s, 1H), 6.43 (d, J = 2.3 Hz, 2H).

^{13}C NMR (126 MHz, CDCl$_3$) δ 155.54, 149.97, 137.59, 132.22, 130.40, 129.06, 124.81, 122.90, 121.97, 119.17, 116.21, 53.88.

MS (EI): m/z (%) = 643.8 [18], 645.8 [68], 647.8 [M$^+$, 100], 649.8 [66], 650.8 [17].

2,2′,7,7′-Tetrakis(*N*,*N*-di(4-methoxyphenyl)amino)-spiro-(fluorene-9,9′-xanthene) (SFX-MeOTAD)

Method A. A mixture of 2,2′,7,7′-tetrabromo-spiro(fluorene-9,9′-xanthene) (0.200 g, 0.309 mmol), 4,4′-dimethoxydiphenylamine (0.425 g, 1.852 mmol), Pd$_2$(dba)$_3$ (0.057 g, 0.062 mmol), tri(*o*-tolyl)phosphine (0.113 g, 0.371 mmol), sodium *tert*-butoxide (0.178 g, 1.852 mmol) were added to a oven dried Schlenk tube and dried under vacuum for 2 hours. Dry toluene (4 mL) was added and the mixture was stirred under nitrogen at 110 °C for 20 hours. The solution was diluted with toluene filtered through Celite and extracted with water. The organic layer was dried over anhydrous sodium sulfate, filtered and the solvent was remove on rotary evaporator. The residue was purified by column chromatography (SiO$_2$, eluent: acetone/hexane 1/8, 1/5, 1/4, v/v) and then precipitated from a solution of acetone into an excess of methanol. The precipitate was filtered off and washed with methanol to give 0.232 g (60%) as a yellowish solid.

Method B. A mixture of 2,2′,7,7′-tetrabromo-spiro(fluorene-9,9′-xanthene) (7 g, 10.803 mmol), 4,4′-dimethoxydiphenylamine (12.384 g, 54.014 mmol), Pd(OAc)$_2$ (0.048 g, 0.216 mmol), sodium *tert*-butoxide (6.227 g, 64.818 mmol) and tri-*tert*-butylphosphonium tetrafluoroborate (0.125 g, 0.432 mmol) were added to a oven dried Schlenk tube and dried under vacuum for 2 hours. Dry toluene (100 g mL) was added and the mixture was stirred under nitrogen at 110 °C for 20 hours. The solution was diluted with toluene (250 mL) filtered through silica plug (26 g) and washed with AcOEt (300 mL). It was extracted with water and organic phase was dried over anhydrous magnesium sulfate, filtrated and concentrated on rotary evaporator. The residue was purified by column chromatography (SiO$_2$, 26 g, eluent: acetone/hexane 5.5 L/1.1 L, 4 L/1 L, 2.7 L/0.9 L) and then precipitated from a solution of acetone (750 mL) into methanol (1.5 L). Then concentrated on rotary evaporator to 0.5 L and the precipitate was filtered off and washed with methanol (300 mL) to give 9.540 g (71%) as a yellowish solid. 2.568 g of 4,4′-dimethoxydiphenylamine was recovered from the first fractions of column.

Elemental analysis (%). Calculated for C$_{81}$H$_{68}$N$_4$O$_9$: C 78.37, H 5.52, N 4.51. Result: C 78.40, H 5.43, N 4.46.

^{1}H NMR (500 MHz, benzene-d$_6$) δ 3.28 (s, 12H), 3.31 (s, 12H), 6.65–6.71 (m, 8H), 6.73–6.77 (m, 8H), 6.82 (dd, J = 8.8, 2.7 Hz, 2H), 6.86 (d, J = 2.6 Hz, 2H), 6.88–6.94 (m, 10H), 6.97 (d, J = 8.8 Hz, 2H), 7.00–7.05 (m, 8H), 7.09 (d, J = 8.3 Hz, 2H), 7.42 (d, J = 2.1 Hz, 2H).

^{13}C NMR (126 MHz, benzene-d$_6$) δ 55.0, 55.0, 114.9, 115.1, 118.0, 118.9, 120.4, 122.0, 122.1, 123.9, 125.3, 126.3, 127.2, 128.0, 128.2, 128.4, 133.4, 141.8, 142.1, 144.5, 147.8, 148.5, 155.2, 155.7, 156.2.

MS (ESI): m/z (%) = 1241.5 [(M + H)$^+$, 100].

2,2′,7,7′-Tetrakis(*N,N*-diphenylamino)-spiro(fluorene-9,9′-xanthene) (SFX-TAD). The same protocol as for **SFX-MeOTAD** (Method B).

Product was obtained as a colourless solid 0.388 g (56%).

Elemental analysis (%). Calculated for $C_{73}H_{52}N_4O$: C 87.57, H 5.23, N 5.60. Result: C 87.53, H 5.18, N 5.68.

^{1}H NMR (601 MHz, methylene chloride-d_2) δ = 6.38 (d, J = 2.6, 2H), 6.84–7.01 (m, 32H), 7.14–7.21 (m, 16H), 7.39 (d, J = 8.2, 2H).

^{13}C NMR (151 MHz, methylene chloride-d_2) δ 54.0, 54.7, 118.3, 120.7, 121.3, 122.6, 123.2, 123.2, 124.4, 124.7, 125.5, 125.6, 126.9, 129.6, 129.7, 134.6, 143.1, 147.9, 148.0, 148.2, 148.3, 156.8.

MS (ESI): m/z (%) = 1000.41 [(M)$^+$, 100].

2,2′,7,7′-Tetrakis(*N*-phenothiazylo)-spiro(fluorene-9,9′-xanthene) (SFX-TPTZ). The same protocol as for **SFX-MeOTAD** (Method B) except product was purified by crystallization toluene/chlorobenzene mixture.

Product was obtained as a beige solid 0.300 g (35%).

Elemental analysis (%). Calculated for $C_{73}H_{44}N_4OS_4$: C 78.19, H 3.95, N 5.00. Result: C 78.08, H 4.00, N 5.13.

^{1}H NMR (601 MHz, methylene chloride-d_2) δ = 5.92 (dd, J = 8.3, 1.2, 4H), 6.02 (dd, J = 8.3, 1.2, 4H), 6.41 (ddd, J = 8.3, 7.3, 1.6, 4H), 6.55 (ddd, J = 8.2, 7.4, 1.6, 4H), 6.72 (m, 10H), 6.96 (ddd, J = 8.9, 7.6, 1.5, 8H), 7.26 (dd, J = 8.7, 2.5, 2H), 7.40–7.43 (m, 4H), 7.50 (d, J = 8.7, 2H), 8.03–8.05 (m, 2H).

^{13}C NMR (151 MHz, methylene chloride-d_2) δ 54.0, 55.1, 115.8, 116.3, 120.0, 120.3, 120.5, 123.0, 123.1, 123.6, 126.4, 127.1, 127.1, 127.8, 128.4, 130.6, 132.0, 132.5, 136.8, 139.2, 142.1, 144.6, 144.8, 151.2, 158.3, 206.9.

MS (ESI): m/z (%) = 1120.24 [(M)$^+$, 30].

2,2′,7,7′-Tetrakis(*N,N*-carbazolo)-spiro(fluorene-9,9′-xanthene) (SFX-TCz). The same protocol as for **SFX-MeOTAD** (Method B).

Product was obtained as a colourless solid 0.571 g (83%).

Elemental analysis (%). Calculated for $C_{73}H_{44}N_4O$: C 88.28, H 4.47, N 5.64. Result: C 88.14, H 4.54, N 5.51.

^{1}H NMR (500 MHz, methylene chloride-d_2) δ = 6.95 (dd, J = 2.1, 0.8, 2H), 7.15 (dt, J = 8.1, 0.9, 4H), 7.19–7.40 (m, 20H), 7.45–7.51 (m, 4H), 7.63 (dd, J = 8.0, 1.9, 2H), 7.68 (m, J = 1.65, 2H), 7.99 (dd, J = 8.0, 0.6, 2H), 8.08 (ddd, J = 7.7, 1.4, 0.7, 4H), 8.15 (dt, J = 7.7, 1.0, 4H).

^{13}C NMR (126 MHz, methylene chloride-d_2) δ 54.0, 54.9, 109.8, 110.2, 119.4, 120.4, 120.7, 120.8, 120.9, 122.7, 123.6, 124.0, 124.7, 124.8, 126.6, 126.6, 127.7, 128.0, 128.5, 133.6, 138.5, 138.6, 141.3, 141.4, 150.4, 158.0.

MS (ESI): m/z (%) = 992.35 [(M)$^+$, 30].

4.8 Perovskite solar cell fabrication and characterisation

The mesoporous Al_2O_3 based perovskite ($CH_3NH_3PbI_{3−x}Cl_x$) solar cells have been fabricated as reported in literature[32,33] with slight modification.[30] Briefly, fluorine-doped tin oxide coated glass substrates (FTO, 7 Ω sq^{-1}, Solaronix) were etched with zinc powder and HCl (4 M aqueous solution) to give the desired electrode patterning. The patterned substrates were cleaned with Hellmanex (2% by volume in de-ionized water) and then sequentially ultrasonicated in de-ionized water, acetone, and methanol. Oxygen plasma cleaning was then used to remove the last traces of organics. A 50 nm blocking layer of TiO_2 was then deposited by spin coating (speed 2000 rpm, 2000 rpm s^{-1} ramp) a weakly acidic solution of titanium isopropoxide in ethanol (350 μL in 5 mL ethanol with 0.013 M HCl), and annealed at 500 °C for 30 min. A 400 nm of mesoporous Al_2O_3 layer was deposited by spin-coating (speed 2500 rpm, ramp 2500 rpm s^{-1}, time 60 s) a colloidal dispersion of <50 nm Al_2O_3 nanoparticles (Sigma-Aldrich, CAS number 702129) in isopropanol (1 : 2 by volume), followed by drying at 150 °C for 10 min to remove any residual isopropanol. The perovskite was deposited in nitrogen filled glovebox (with <30% relative humidity) by spin coating (speed 2000 rpm, ramp 2000 rpm s^{-1}) a 40 wt% DMF solution of methylammonium iodide (synthesized as reported in literature) and PbCl$_2$ (3 : 1 molar ratio). The substrate is then heated to 100 °C for 2 hours on a hotplate in nitrogen filled glovebox after DMF solvent annealing. The hole-transport layer was deposited by spin coating an 8.5 vol% **spiro-MeOTAD** (or **SFX-MeOTAD**) in chlorobenzene solution with the standard additives 0.8 mM *tert*-butylpyridine and 20 mM lithium bis(trifluoromethanesulfonyl) imide (from 0.61 M acetonitrile solution). Gold electrodes (~50 nm) were then deposited by evaporation under high vacuum through a shadow mask.

The current–voltage (*I–V*) curves were measured (Potentiostat/Galvanostat, Metrohm Autolab B.V.) under simulated AM 1.5 sunlight at 100 mW cm^{-2} irradiance generated by a Class AAA small collimated Beam Solar simulator (SF300A, Sciencetech Inc.), with the intensity calibrated by Si reference cell. The mismatch factor between the simulated sunlight and the actual solar spectrum is not corrected. The solar cells were masked with a metal aperture to define the active area, typically 0.06–0.09 cm^{-2}. Hitachi 470011 cold field-emission scanning electron microscope has been utilised to do the cross-section SEM of the PSCs.

The hole conductivity measurements have been carried out using two probe method for the **spiro-MeOTAD** and **SFX-MeOTAD** films [with standard additives of 0.8 mM *tert*-butylpyridine and 20 mM lithium bis(trifluoromethanesulfonyl)imide (from 0.61 M acetonitrile solution)] deposited on p = doped Si wafer with SiO$_2$ (100 nm) coating and electrode consisting of Cr (5 nm) and Au (50 nm) 1 mm in width and separated by 0.03 mm.

Acknowledgements

Notes and references

1 A. Kojima, K. Teshima, Y. Shirai and T. Miyasaka, *J. Am. Chem. Soc.*, 2009, **131**, 6050–6051.

2 M. Grätzel and A. Hagfeldt, http://www.dyesol.com/media/wysiwyg/Documents/2015-asx-announcements/2015-12-08-DYE0397_-_EPFL_achieves_21_efficiency.pdf.

4862 | *J. Mater. Chem. A*, 2016, **4**, 4855–4863

This journal is © The Royal Society of Chemistry 2016

3 P. Gratia, A. Magomedov, T. Malinauskas, M. Daskeviciene, A. Abate, S. Ahmad, M. Grätzel, V. Getautis and M. K. Nazeeruddin, *Angew. Chem., Int. Ed.*, 2015, **54**, 11409–11413.

4 F. Zhang, X. Yang, M. Cheng, J. Li, W. Wang, H. Wang and L. Sun, *J. Mater. Chem. A*, 2015, **3**, 24272–24280.

5 K. Rakstys, A. Abate, M. I. Dar, P. Gao, V. Jankauskas, G. Jacopin, E. Kamarauskas, S. Kazim, S. Ahmad, M. Grätzel and M. K. Nazeeruddin, *J. Am. Chem. Soc.*, 2015, **137**, 16172–16178.

6 S. Park, J. H. Heo, C. H. Cheon, H. Kim, S. H. Im and H. J. Son, *J. Mater. Chem. A*, 2015, **3**, 24215–24220.

7 M. L. Petrus, T. Bein, T. J. Dingemans and P. Docampo, *J. Mater. Chem. A*, 2015, **3**, 12159–12162.

8 A. Abate, M. Planells, D. J. Hollman, V. Barthi, S. Chand, H. J. Snaith and N. Robertson, *Phys. Chem. Chem. Phys.*, 2015, **17**, 2335–2338.

9 Y. Song, S. Lv, X. Liu, X. Li, S. Wang, H. Wei, D. Li, Y. Xiao and Q. Meng, *Chem. Commun.*, 2014, **50**, 15239–15242.

10 L.-H. Xie, F. Liu, C. Tang, X.-Y. Hou, Y.-R. Hua, Q.-L. Fan and W. Huang, *Org. Lett.*, 2006, **8**, 2787–2790.

11 M. Sun, R. Xu, L. Xie, Y. Wei and W. Huang, *Chin. J. Chem.*, 2015, **33**, 815–827.

12 M. Pietraszkiewicz, M. Maciejczyk, I. D. W. Samuel and S. Zhang, *J. Mater. Chem. C*, 2013, **1**, 8028–8032.

13 X. Zhao, Y. Wu, N. Shi, X. Li, Y. Zhao, M. Sun, D. Ding, H. Xu and L. Xie, *Chin. J. Chem.*, 2015, **33**, 955–960.

14 N. Cocherel, C. Poriel, L. Vignau, J.-F. Bergamini and J. Rault-Berthelot, *Org. Lett.*, 2010, **12**, 452–455.

15 J.-F. Gu, G.-H. Xie, L. Zhang, S.-F. Chen, Z.-Q. Lin, Z.-S. Zhang, J.-F. Zhao, L.-H. Xie, C. Tang, Y. Zhao, S.-Y. Liu and W. Huang, *J. Phys. Chem. Lett.*, 2010, **1**, 2849–2853.

16 Z. Chu, D. Wang, C. Zhang, F. Wang, H. Wu, Z. Lv, S. Hou, X. Fan and D. Zou, *Synth. Met.*, 2012, **162**, 614–620.

17 B. E. Koene, D. E. Loy and M. E. Thompson, *Chem. Mater.*, 1998, **10**, 2235–2250.

18 B. A. Kamino, B. Mills, C. Reali, M. J. Gretton, M. A. Brook and T. P. Bender, *J. Org. Chem.*, 2012, **77**, 1663–1674.

19 W.-F. Jiang, H.-L. Wang, A.-G. Wang and Z.-Q. Li, *Synth. Commun.*, 2008, **38**, 1888–1895.

20 J. Pei, J. Ni, X.-H. Zhou, X.-Y. Cao and Y.-H. Lai, *J. Org. Chem.*, 2002, **67**, 4924–4936.

21 K. Zhang, L. Wang, Y. Liang, S. Yang, J. Liang, F. Cheng and J. Chen, *Synth. Met.*, 2012, **162**, 490–496.

22 I. K. Ding, J. Melas-Kyriazi, N. Le Cevey-Ha, K. G. Chittibabu, S. M. Zakeeruddin, M. Grätzel and M. D. McGehee, *Org. Electron.*, 2010, **11**, 1217–1222.

23 A. Murray, J. M. Frost, C. Hendon, C. D. Molloy, D. Carbery and A. Walsh, *Chem. Commun.*, 2015, **51**, 8935–8938.

24 N. Joong Jeon, H. Geun Lee, Y. Chan Kim, J. Seo, J. Hing Noh, J. Lee and S. Il Seok, *J. Am. Chem. Soc.*, 2014, 7837.

25 W. Rettig, *Appl. Phys. B: Photophys. Laser Chem.*, 1988, **45**, 145–149.

26 J. Catalán, C. Díaz, V. López, P. Pérez and R. M. Claramunt, *J. Phys. Chem.*, 1996, **100**, 18392–18398.

27 P. Ganesan, K. Fu, P. Gao, I. Raabe, K. Schenk, R. Scopelliti, J. Luo, L. H. Wong, M. Grätzel and M. K. Nazeeruddin, *Energy Environ. Sci.*, 2015, **8**, 1986–1991.

28 H. J. Snaith and M. Grätzel, *Appl. Phys. Lett.*, 2006, **89**, 262114.

29 A. Abate, D. R. Staff, D. J. Hollman, H. J. Snaith and A. B. Walker, *Phys. Chem. Chem. Phys.*, 2014, **16**, 1132–1138.

30 Z. Xiao, Q. Dong, C. Bi, Y. Shao, Y. Yuan and J. Huang, *Adv. Mater.*, 2014, **26**, 6503–6509.

31 N. Ahn, D.-Y. Son, I.-H. Jang, S. M. Kang, M. Choi and N.-G. Park, *J. Am. Chem. Soc.*, 2015, **137**, 8696–8699.

32 J. M. Ball, M. M. Lee, A. Hey and H. J. Snaith, *Energy Environ. Sci.*, 2013, **6**, 1739.

33 M. M. Lee, J. Teuscher, T. Miyasaka, T. N. Murakami and H. J. Snaith, *Science*, 2012, **338**, 643–647.

34 A. Krishna, D. Sabba, H. Li, J. Yin, P. P. Boix, C. Soci, S. G. Mhaisalkar and A. C. Grimsdale, *Chem. Sci.*, 2014, **5**, 2702.

35 Y. Song, S. Lv, X. Liu, X. Li, S. Wang, H. Wei, D. Li, Y. Xiao and Q. Meng, *Chem. Commun.*, 2014, **50**, 15239–15242.

36 T. Leijtens, I.-K. Ding, T. Giovenzana, J. T. Bloking, M. D. McGehee and A. Sellinger, *ACS Nano*, 2012, **6**, 1455–1462.

37 C. M. Cardona, W. Li, A. E. Kaifer, D. Stockdale and G. C. Bazan, *Adv. Mater.*, 2011, **23**, 2367–2371.

This journal is © The Royal Society of Chemistry 2016

J. Mater. Chem. A, 2016, **4**, 4855–4863 | **4863**